UC Santa Barbara
UC Santa Barbara Previously Published Works

Title

Methods and Protocols: Practical Magnetic Measurement

Permalink

Journal

ISSN

Authors

Mozur, Eve M
Seshadri, Ram

Publication Date

DOI

Peer reviewed

Methods and Protocols: Practical Magnetic Measurement

Eve M. Mozur[*,†] and Ram Seshadri[*,‡]

†*Department of Metallurgical and Materials Engineering*

Colorado School of Mines, Golden, Colorado 80401, United States

‡*Materials Department and Materials Research Laboratory*

University of California, Santa Barbara, California 93106, United States

E-mail: evemozur@mines.edu; ramseshadri@ucsb.edu

Abstract

Magnetic materials are useful in myriad ways, playing a critical role in modern society. Magnetic measurements however, serve a much larger purpose than solely characterizing magnetic materials. Information obtained from magnetic measurements is essential across a wide swathe of materials, ranging from topological quantum materials to catalysts and battery materials. As with many advanced characterization and measurement techniques, practical aspects of magnetic measurements requires experience that is not readily gained from textbooks and user manuals. As one example, the nature of the measurement and the interpretation of data can be strongly sample-dependent and appropriate experimental design is essential to obtain reliable results in an efficient manner. In this "Methods and Protocols" contribution, we seek to demystify magnetic measurements for non-experts, discussing best practices for a range of different magnetic measurements with illustrative examples.

Introduction

Magnetism is a fundamental property of molecules and materials, making magnetic characterization a powerful probe with great versatility. Magnetometry is often considered to be a tool that is employed to establish magnetic ground states associated with ferro or antiferromagnetic order, the formation of skyrmion order, spin canting, frustrated magnetic states, *etc.*[1–4] However, magnetometry can also provide provide insights into a diverse range of materials and applications where magnetic ground states are not the principal function. For example, magnetometry can be employed to characterize changes in the electron count of battery materials during cycling,[5] and can help measure the entropy change through a magnetic transition, which is essential for the screening magnetocaloric materials.[6]

The diversity of magnetic characterization techniques makes it difficult to be an expert in the field as a whole. However, the versatility of what one can learn means that even non-specialists can gain remarkable insight from a carefully conducted experiment. The purpose of this contribution is to bridge the gap between the concepts described in textbooks and the results shown in the literature. Therefore, we will not discuss the fundamental physics of magnetism; for this we recommend *Introduction to Magnetic Materials*[7] or the section on magnetism in the recent text *Solid State Materials Chemistry*.[8] Instead, we will focus on the practical side of magnetic measurements, particularly on experimental design with modern instrumentation. The topic of molecular magnets is rich and thriving, but is outside the scope of this contribution and interested readers are pointed to recent review from Chilton.[9] While the measurement techniques described here are pertinent for superparamagnetic, ferromagnetic, and antiferromagnetic nanoparticles, they are not explicitly discussed here, and other resources will complement this contribution.[10]

We begin by discussing magnetic units, followed by sample preparation, and review the basics of setting up a magnetic measurement. With this foundation, we discuss one of the most common uses for magnetic measurements, the characterization of magnetic

behavior through temperature and field-dependent experiments. The section that follows describes the process for calculating a change in entropy over a magnetic phase transition from temperature-dependent magnetization measurements. After a survey of magnetic measurement methods, we describe the characterization of relevant materials including spin glasses and superconductors through magnetometry. We end with a brief discussion of complementary techniques, focusing on Mössbauer spectroscopy and neutron diffraction. This last section is not meant as a tutorial, but a suggestion of experiments to explore when magnetometry leaves unanswered questions.

Practical units in magnetic measurements

Different domains of inquiry have historically used different magnetic units. Here, we describe the units that are commonly preferred by materials chemists and some context for their use, as summarized in Table 1.[11] Typically, CGS units are preferred over SI. The magnetic field seen by the sample is represented by H, and is best reported in Oersted (Oe) or kiloOersted (kOe). For high magnetic fields, the unit Tesla (T) is also employed in the literature, and $1\,\mathrm{T} = 10^4\,\mathrm{Oe}$. In SI units, the correct description is $\mu_0 H$ rather than simply H, where μ_0 is the permittivity of a vacuum.

Applying a field to a sample will lead to a response, which is the magnetization (M) that is reported in electromagnetic units (emu) and is the form of data output by most magnetometers. To be able to compare across studies the magnetization can be converted to a susceptibility ($\chi = \mathrm{d}M/\mathrm{d}H \approx M/H$) through normalizing to the applied field on a *per* mole basis. The CGS units of the molar χ are $\mathrm{emu}\,\mathrm{mol}^{-1}\,\mathrm{Oe}^{-1}$. The susceptibility is often also reported in units of the inverse volume (cm^{-3}) rather than on a per mole basis. For the types of analyses we discuss here, the molar χ helps relate back to the materials chemistry. In some cases, it is more informative to report magnetization in Bohr magnetons (μ_B) per formula unit or *per* magnetic atom. The conversion between emu and μ_B is based on the

3

definition

$$\mu_B = \frac{eh}{4\pi m_e c} \tag{1}$$

where e is the charge of an electron, h is the Planck constant, m_e is the electron mass and c is the speed of light. A convenient multiplicative factor is though the conversion $5584 \, \mathrm{emu} \, \mathrm{mol}^{-1} = 1 \, \mu_B$ *per* formula unit. This conversion is usually applicable to the saturation (*i.e.*, high-field) magnetization of a ferromagnetic or a ferrimagnet, well below the magnetic ordering temperature. Note that this conversion of the magnetization to a magnetic moment should not be confused with the effective magnetic moment (μ_{eff}) extracted from Curie-Weiss fits to paramagnets, discussed later.

Table 1: Summary of practical magnetic units.

variable	definition	units
H	field seen by sample	Oe, kOe
M	magnetic response of sample, magnetization	emu
χ	molar magnetic susceptibility of the sample	$\mathrm{emu} \, \mathrm{mol}^{-1} \, \mathrm{Oe}^{-1}$

Experimental details

Sample preparation

This section discusses general concerns for the preparation of solid samples, as appropriate for modern, widely deployed magnetometers such as a superconducting quantum interference device (SQUID) magnetometer. The sample preparation process is summarized in Figure 1.

Magnetic measurements begin from the moment one pulls out the reagents. With magnetic materials, sample contamination can dramatically impact observed results. For example, in hafnium oxide films, contamination from metal tweezers led to an erroneous assignment of a ferromagnetic phase.[12] These types of environmental impurities can greatly
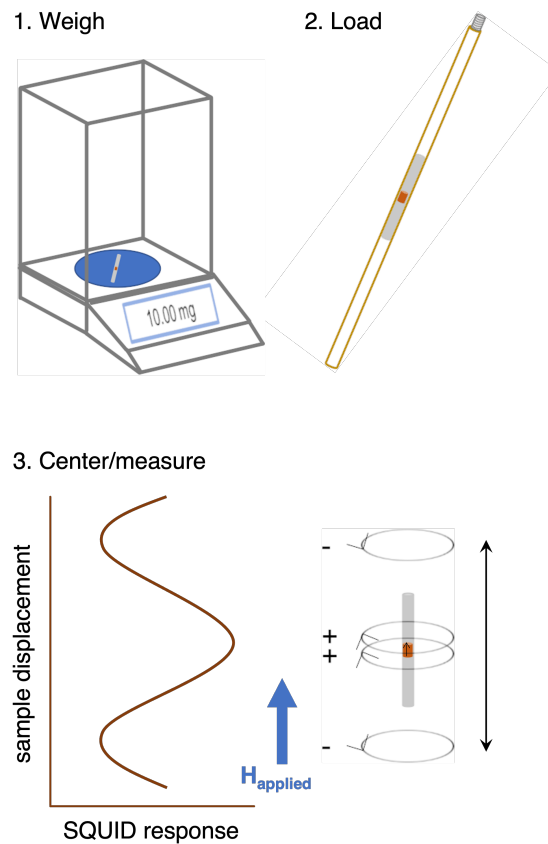
Figure 1: Sample preparation for a typical magnetic measurement. Samples must first be precisely weighed in an appropriate sample container. Sample containers can be mounted on a brass or silica rod, plastic straw, or ceramic paddle depending on the sample and temperature range of interest. The first step after loading the sample into the instrument is centering the sample within the detection coils. During centering, a magnetic field ($H_{applied}$) polarizes the magnetic moments within the sample. As the polarized sample moves through the detection coils, an electric field is generated according to Lenz's Maw. The maximum detected signal indicates the sample position.

contribute to the measured magnetization during data collection for materials with small magnetic responses, including paramagnets and antiferromagnets. Platinum is a known paramagnet without an ordering temperature down to temperatures below $2\,\mathrm{K}$,[13] but a bump can be see in the temperature-dependent susceptibility collected for this contribution near $T = 50\,\mathrm{K}$ in Figure 2. The shape of this feature suggests an antiferromagnetic impurity, although the identity of the other material is unclear.
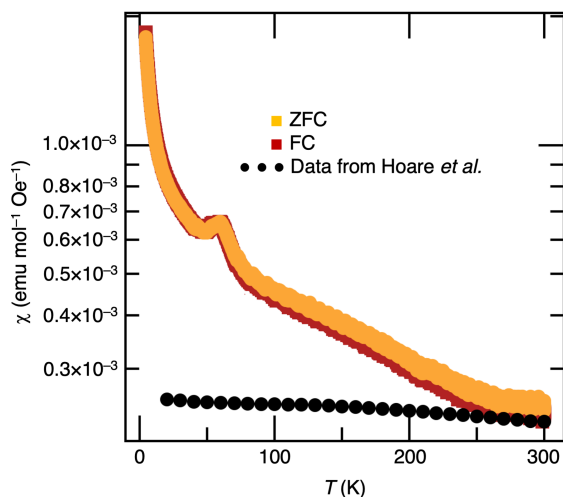

Figure 2: Susceptibility as a function of temperature for platinum metal. Platinum metal is a Pauli paramagnet[14] and therefore should exhibit temperature independent susceptibility as previously reported by Hoare *et al.* and plotted as black circles. However, the data collected both under ZFC and FC conditions here show clear temperature dependence and a transition near $T = 50\,\mathrm{K}$. These anomalies indicate the presence of an environmental impurity.

The ideal sample mass to load for a measurement depends on the sample magnetization. In all cases, however, knowing an accurate sample mass is imperative for extracting parameters per formula unit. For materials with high magnetizations, a large sample mass could lead to a signal which is high enough to saturate the detector. Conversely, if too small a sample mass of a low magnetization material is measured, the signal might be below the detection limits, or the signal could be dominated by environmental impurities. For a previously uncharacterized material, masses between $10\,\mathrm{mg}$ and $20\,\mathrm{mg}$ are good starting point for measurement on SQUID magnetometers. Strong ferromagnets and supercon-

ductors will require masses as small as 3 mg. The accuracy of measurement will increase as the sample volume and shape approaches those of the standards used to calibrate the instrument.

With the correct sample holder, powders, sintered samples (solid pellets), and single crystals can be loaded and measured. For measurements between $T = 1.8\,\text{K}$ and $T = 370\,\text{K}$, the sample is commonly packed in a polypropylene sample holder that is snapped into a brass sample rod. It is also possible to mount single crystals, films, or sintered samples directly onto a silica rod or paddle using GE varnish or another compatible adhesive. Using a paddle sample holder has the additional benefit of providing the user control over sample orientation with respect to the field. Orientation dependent measurements, although outside the scope of this contribution, are essential for characterizing the magnetic susceptibility along different crystallographic and macroscopic directions.[15,16] This control is particularly important for thin film or single crystalline samples that have anisotropic magnetism and/or structure. Air sensitive samples should be sealed within low-impurity glass or silica ampules. Samples tubes employed in nuclear magnetic resonance (NMR) spectroscopy usually work well for this purpose. For alternating current (AC) and high-field measurements, samples can be embedded within paraffin wax or other low susceptibility, diamagnetic materials in a plastic capsule to prevent particle motion in response to the field. High temperature measurements between $T = 300\,\text{K}$ and $T = 1000\,\text{K}$ using an oven stick require sintered, pressed, or single crystal samples to be mounted onto an alumina sample holder using Zircar cement.

Once the sample is loaded onto the sample holder, one must center the sample within the instrument chamber. During centering, the sample moves completely through the detection coils, several times the distance covered during a measurement the sample (Figure 1). The detection coils are second order gradiometers, which reduce the impact of external, environmental fields. The changing magnetic flux through the detector coils from the moving sample induces a change in the electric field measured by the detection coils.

7

This process necessitates on accurate knowledge of the initial sample position. Inaccurate centering can lead to inaccurate magnetization values.

The first step in centering is to note the general location of the sample when loading the sample into the holder, ensuring that it is close to optimal. The automated centering process can then precisely find the sample through moving it completely and noting the shape of the response as shown in Figure 1. In order generate a magnetic response while centering the sample, a field of anywhere between $H = 200\,\mathrm{Oe}$ and $H\,10\,\mathrm{kOe}$ is applied to the sample at room temperature. Materials with a small magnetization, including antiferromagnets, paramagnets, and small samples, will require a higher field. Centering at low temperature can be helpful for paramagnetic materials or for materials that undergo an ordering transition on cooling to maximize the observable magnetization. If the automated processes do not yield physically meaningful or accurate results, manual centering may be called for. This is done using a knowledge of where the sample is installed on the sample holder. During a temperature or field-dependent measurement, it is may be important to recenter the sample to account for temperature and field effects on the sample.

Setting up a measurement

Types of experiments

Measurements can be divided into two main types, direct current (DC) and alternating current (AC). DC measurements, in which a field is applied and held constant, are more common and are appropriate when dynamics of spins are negligible. AC measurements are often used to supplement DC measurements to gain additional information into magnetic phase transitions, and to understand spin dynamics.[17,18] In an AC measurement, the applied field oscillates between its positive and negative value at a set frequency. At the low frequency limit, this nearly approximates a DC measurement, where the measured magnetization M_{AC} depends on the drive field H_{AC}, the magnetic susceptibility χ, and

time t from the initial pulse as $M_{AC} = \chi H_{AC} \sin(\omega t)$. On increasing the frequency of the oscillating applied field, the magnetic spins can lag behind the magnetic field switching from an irreversible process. This lag manifests as a phase shift in the measured magnetization compared to the phase of the applied field. Typically, this phase shift is expressed as the in-phase magnetic susceptibility, χ', and the out-of-phase magnetic susceptibility, χ''. χ' and χ'' relate to the total magnetic susceptibility as $\chi = \chi' + i\chi''$, and therefore are also commonly referred to as the real susceptibility and the imaginary susceptibility, respectively. χ'' will have a non-zero value if there is any lag of the spins behind the oscillating field.

Sample Demagnitization

In any measurement, it is best practice to assume sample history will have some effect on the magnetic behavior. To avoid a remnant magnetization, it is best to demagnetize the sample by returning to zero field after centering by oscillating the magnetic field, rather than changing the field linearly.

Experimental parameters

There are several important experimental parameters to consider to optimize data collection. We note that this section is focused on SQUID magnetometers equipped with vibrating sample magnetometry (VSM). Here, the sample is vibrated over a relatively small sweep range at a fixed frequency, as in a vibrating sample magnetometer, with AC lock-in detection of the SQUID response providing more reliable measurements.[19] In contrast, previous generations of SQUID instruments used DC detection. These instruments moved the sample slowly though a larger sweep range and measured the manner in which the moving sample and the static magnetic field of the solenoid resulted in a change in the measured DC SQUID response.

The scan length, which is the vertical displacement of the sample though the magne-

tometer during the measurement, should be chosen carefully. Typically, it is best to use a value similar to that used when calibrating the instrument with an external standard. Smaller values improve accuracy and sensitivity by reducing temperature gradients and de-emphasizing any sample heterogeneity, but care should be taken to accurately check the sample centering.

For samples with large magnetizations, the sensitivity offered by small peak amplitudes can swamp the detector, making larger peak amplitudes more appropriate. With large peak amplitudes, it is essential to avoid the sample rod coming into contact with the bottom of the sample chamber to prevent dislodging the sample or damage to the sample holder. In vibrating sample magnetometers (VSM), the peak amplitude will dictate the maximum acceleration of the sample, since instruments tend to use a fixed sample oscillation frequency. Fragile or powder samples may lose integrity at large accelerations.

In most magnetometers, several sample oscillations are averaged together to give a magnetization value. Materials with large magnetizations require shorter scan times, and samples that are weakly magnetic will benefit from more scans per measurement. In some measurements, the number of scans per measurement is controlled by the averaging time, *e.g.* at the set frequency of 40 Hz, a one second averaging time will encompass 4 sample oscillations.

Temperature dependent experiments

For a temperature-dependent measurement, one must decide on a reasonable applied field. Typically, it is best to repeat the measurement at at least two different field strengths to examine any field-dependent phenomena. $H = 100\,\text{Oe}$ or $H = 1\,\text{kOe}$ are reasonable starting points for a material with previously uncharacterized magnetic behavior. Materials with delicate magnetic states that can be quenched by the application of a strong magnetic field, such as skyrmions or superconductors, will only be observable under fields on the order of $H = 100\,\text{Oe}$, but sometimes as small as $H = 5\,\text{Oe}$.[2,20]

Temperature-dependent measurements are typically measured on heating, rather than cooling, since heating allows more accurate sample temperatures. Samples can show different temperature-dependent behavior depending on whether the sample is cooled with no applied field (zero field cooled, ZFC) or under a constant applied field (field cooled, FC). For example, ferromagnets can show a bifurcation between ZFC and FC at the ordering temperature, which indicates energy barriers in domain reorientation.[21] One can understand this behavior through an analogy to heating. Field cooling is analogous to annealing a sample, which tends to lead to more ordered material, while zero field cooling is analogous to quenching a sample. Magnetic domains are more disordered after zero field cooling, with a smaller net magnetization on heating until the system has enough thermal energy to move domain walls.

Field dependent experiments

For a field-dependent measurement, the most important set parameter is the maximum field value. A maximum field of $H = 50\,\mathrm{kOe}$ is achievable with most instruments, and can reveal a large and experimentally relevant section of the magnetic phase diagram at any given temperature. The possibility of metamagnetic (field-driven) states motivates measuring to the highest experimentally feasible field. Typically, field-dependent measurements begin with zero applied field, sweep to a the maximum positive field H_{max}, sweep through zero to $-H_{max}$, and then back through zero to H_{max} in a five quadrant sweep before demagnetizing the sample. This process is important for hard magnetic materials that exhibit hysteresis, as will be addressed in further detail below.

There are additional considerations in an AC experiment. The first is the amplitude, i.e. the maximum value of the applied field. Typical AC measurements use AC fields of several hundred Oersted. The strength of this field is particularly important if one is interested in probing the magnetic ground state to avoid total field polarization or excitation to a higher energy magnetic state. A small amplitude makes it easier to probe magnetic states with

small magnetization, such as skyrmions, and small differences between magnetic states. The second parameter is the frequency of the applied field. Although the most relevant frequencies will depend on the system and physics being probed, a reasonable starting point is between $\nu = 10\,\mathrm{Hz}$ and $\nu = 1\,\mathrm{kHz}$. Understanding is frequently enhanced for many magnetic materials through examining the frequency dependence, in which case a wider range between $\nu = 1\,\mathrm{Hz}$ and $\nu = 1\,\mathrm{kHz}$ can be useful. Frequencies up to $\nu = 10\,\mathrm{kHz}$ may be useful for materials with especially mobile spins. The third parameter is the magnitude of an applied DC field. If this field is set to zero, the magnetic ground state will be probed. The application of an appropriate non-zero field, identified from an DC field-dependent experiment, can allow investigation of metamagnetic (field-driven) states.

Classes of magnetic materials and their measurement

Identification of a diamagnet, paramagnet, ferromagnet, or antiferromagnet

Simple DC experiments are often used to classify the magnetic behavior of a material, whether diamagnetism, paramagnetism, ferromagnetism, or antiferromagnetism, and to identify transitions between magnetic states when they exist. In this section we describe how to best use this type of data to confirm the classification of a material with several informative examples. The analysis of temperature-dependent magnetic susceptibility, particularly the use and limits of the Curie law, have recently been reviewed.[22] We include simple examples of this practice here, and direct readers to this recent contribution for further details.

Magnetically uncorrelated materials

Any material with paired electrons will exhibit diamagnetism. A diamagnet expels magnetic field, leading to a negative magnetic susceptibility and a negative slope in the field-dependent magnetization. Typically, diamagnetism is a weak effect compared to the strong paramagnetic effects from unpaired electrons, and is negligible in materials that have unpaired electrons. If the diamagnetic contribution is non-negligible, one will see a constant negative offset in the temperature-dependent magnetism. The diamagnetic susceptibility contribution can be estimated by $\chi_{dia} \approx -10^6 \times (m_{mol}/2)\,\mathrm{emu\,mol^{-1}\,Oe^{-1}}$ where m_{mol} is the molar mass of the material in question.
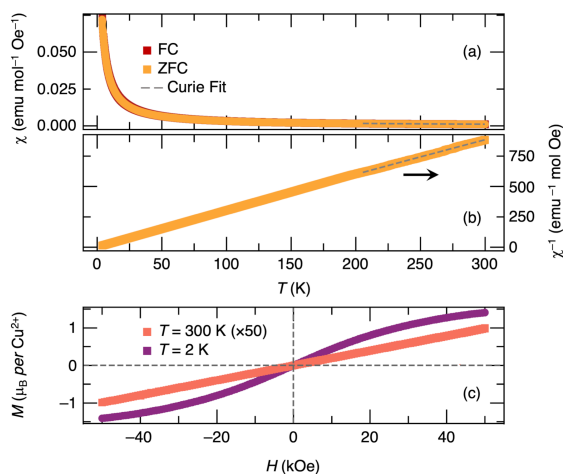
Figure 3: (a) Magnetic susceptibility vs. temperature for $CuSO_4 \cdot 5\,H_2O$ collected under a H = 1 T applied field after cooling under zero field, ZFC, and after cooling under a H = 1 T field, FC. The ZFC and FC datasets overlay nearly perfectly, indicating negligible irreversibility. (b) Inverse susceptibility fit to the Curie law (c) Magnetization vs. applied field for $CuSO_4 \cdot 5\,H_2O$ at 300 K and 2 K. The T = 300 K data have been magnified by a factor of 50.

The field-dependent magnetization of a paramagnet has the opposite sign to a that of a diamagnet. Rather than expelling an applied magnetic field, the unpaired spins of a paramagnet will tend to align in the direction of the external field. In most paramagnets thermal energy drives the random fluctuations of the spins. As thermal energy is removed and entropy becomes less heavily weighted in the free energy, its spins are more likely to align in the direction of the applied magnetic field. The magnetization and susceptibility of

a paramagnet are therefore larger in magnitude at low temperature than at high temperature, as shown in Figure 3a for $CuSO_4 \cdot 5\,H_2O$. The inverse susceptibility of a paramagnet will be linear, and intercept the origin (Figure 3b). The temperature-dependent magnetic susceptibility of a paramagnet can be described with the Curie law:

$$\chi = \frac{C}{T} + \chi_0 \tag{2}$$

where χ_0 is the diamagnetic susceptibility, T is temperature, C is the Curie constant which is known to have the form:

$$C = \frac{N_A \mu_B^2 \mu_{eff}^2}{3 k_B} \approx \frac{\mu_{eff}^2}{8} \tag{3}$$

where N_A is Avogadro's number, k_B is the Boltzmann constant, μ_{eff} is the effective moment, and μ_B is the Bohr magneton. By fitting the susceptibility or the inverse susceptibility to the Curie law, as shown in Figure 3b, one can extract the Curie constant as a metric of how many unpaired electrons contribute to the magnetic moment. It is best practice to exclude the lower temperature data where spin correlations are stronger from these fits, weighting the fit to data at temperatures well above the upturn, in this case above $200\,K$. The fit shown in Figure 3b gives $C = 0.33\,\mathrm{emu\,K\,mol^{-1}\,Oe^{-1}}$, and $\chi_0 = -5.73 \times 10^{-6}\,\mathrm{emu\,mol^{-1}\,Oe^{-1}}$. From this value of C we calculate a μ_{eff} of $1.62\,\mu_B$. We can compare this effective value to the expected value based on the spin quantum number. In copper sulfate pentahydrate, copper has one unpaired electron, so $S = \frac{1}{2}$ and the effective moment is expected to be equal to the spin-only value given by $2\sqrt{S(S+1)} = 1.7$. In this case our expected and calculated value are quite close, indicating that copper sulfate hydrate can be considered a spin only system, rather than a spin-orbit coupled system.

As the magnitude of the external field increases, more spins will align in the direction of the field, increasing the overall magnetization as shown for $CuSO_4 \cdot 5\,H_2O$ at room temperature and at $2\,K$ in Figure 3c. As expected from Figure 3a, the low temperature

measurement exhibits a much higher magnetization. Additionally, at lower temperature the field-dependent magnetization can look more "S" shaped than linear, as Brillouin behavior becomes more apparent. Note that there is no plateau in the high field region, as the maximum magnetization continues to increase. The field-dependent magnetization is plotted either in units of $emu\,mole^{-1}$, or as we have done in Figure 3c, as μ_B per formula unit. The latter unit can give some insight into the number of spins that align with the applied field. At high field and low temperature, the magnetization of $CuSO_4 \cdot 5\,H_2O$ is close to the $1\,\mu_B$ per Cu^{2+} expected for a single spin. Note that the low-temperature magnetization in μ_B per magnetic ion should correspond to the total number of spins per magnetic ion, and is not to be considered as the same as μ_{eff}.

Temperature-dependent paramagnetism hinges on the presence of localized spins. Temperature -independent paramagnetism occurs in Pauli paramagnets and Van Vleck paramagnets. Most metals are Pauli paramagnets, where electrons are delocalized within the conduction band. Upon application of a field, the energy of the spin up and spin down electrons within the conduction band diverges, leading to a net magnetic magnetization as the spins flip to reduce their energy. Pauli paramagnets have a small magnetization relative to typical paramagnets and the susceptibility is temperature-independent. Van Vleck paramagnetism occurs in materials that have paired electrons but that have low-lying excited states that are paramagnetic. In $KMnO_4$, the manganese is formally in the 7+ oxidation state, meaning that it has no unpaired d electrons. One would therefore expect a diamagnetic response. However, this material has a positive magnetic susceptibility, that appears relatively constant between $T = 300\,K$ and $T = 440\,K$.[23] Here, the magnetic response comes from ligand to metal electron transfer, where electrons formally belonging to oxygen are thermally excited into the empty manganese d orbitals.[24] This effect is temperature independent as the relevant energy levels are much less than $k_B T$.

Determining if the material is diamagnetic, paramagnetic or Pauli paramagnetic provides insight into the charge state of the magnetic ion. In the potential lithium ion cathode

PNb$_9$O$_{25}$, lithiation leads to a transition from temperature-dependent paramagnetism to temperature independent paramagnetism. The temperature independent magnetism was assigned as Pauli paramagnetism and confirms the metal to insulator transition from reduction of the niobium during lithiation.[5]

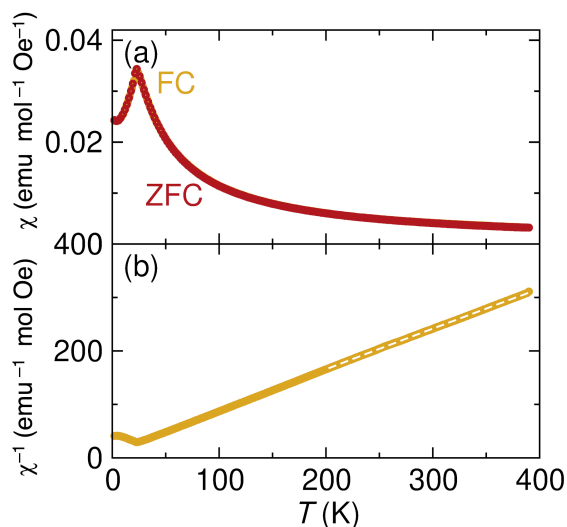## Magnetically correlated materials

Figure 4: (a) Magnetic susceptibility as a function of temperature for NiTiO$_3$ collected under a 1 T applied field after cooling under zero field, ZFC, and after cooling under a 1 T field, FC. (c) Inverse susceptibility fit to the Curie law. Data were originally presented in Harada 2016.[25]

Long-range correlations between spins will change the field and temperature-dependent magnetic response. For an antiferromagnet, where magnetic spins anti-align upon ordering, the lack of a net magnetization leads to field-dependent behavior that looks very similar to that of paramagnets. Therefore, we must rely on temperature-dependent data sets to reliably identify antiferromagnets. At the transition temperature between the paramagnetic and antiferromagnetic state, known as the Néel temperature (T_N), the temperature-dependent susceptibility will exhibit a maximum before decreasing in magnitude as spins anti-align with each other, as seen near 22 K for NiTiO$_3$ in Figure 4a. Similarly the inverse

susceptibility χ^{-1} is linear above the Néel temperature, with a discontinuity and change in slope below the Néel temperature (Figure 4b).

One can fit the paramagnetic regime of the susceptibility of a correlated material with the a modified version of the Curie law known as the Curie-Weiss law,

$$\chi = \frac{C}{T - \Theta_{CW}} + \chi_0 \tag{4}$$

which incorporates the Curie-Weiss temperature (Θ_{CW}) as an effective field describing all spin-spin interactions (magnetic correlations) in a simplified manner. Antiferromagnets have negative values for Θ_{CW}, since spins are anti-correlated. When using the Curie-Weiss law, it is essential to only model the paramagnetic regime, as the Curie-Weiss law only describes paramagnetism. In practice, the lowest temperature involved in a Curie-Weiss fit should be at least $50\,K$ above any ordering temperature; in $NiTiO_3$ we consider only the data above $T = 200\,K$. Based on the fit in shown in Figure 4b, $NiTiO_3$ has a value for C of $1.3\,\mathrm{emu\,K\,mol^{-1}\,Oe^{-1}}$, and a $\Theta_{CW} = -14\,K$ which is not very far from the measure $T_N = 22\,K$ at long-range antiferromagnetic order is found.[25] From the value of C, we calculate an effective moment of $3.2\,\mu_B$, which is slightly higher than that expected for nickel (II) ($2\sqrt{S \times (S+1)} = 2\sqrt{1 \times (1+1)} = 2.8$) indicating an orbital contribution.

At the transition from a paramagnetic state to a ferromagnetic state, magnetic spins align parallel, leading to a dramatic increase in the measured magnetization. This transition is evident in the temperature-dependent susceptibility in both MnPdGa and MnPtGa at the paramagnetic to ferromagnetic transition temperature, called the Curie temperature T_C, near $310\,K$ in MnPdGa and $225\,K$ in MnPtGa (Figures 5a, 6a). Additionally, in MnPdGa the temperature-dependent data show an anomaly near $T = 125\,K$ (Figure 5b). This feature suggests an additional magnetic transition, although it is not clear what type of transition this feature represents from this dataset.

Unlike a paramagnet, where the FC and ZFC data typically overlay, materials with correlated spins can exhibit bifurcation of FC and ZFC data below the transition temperature.
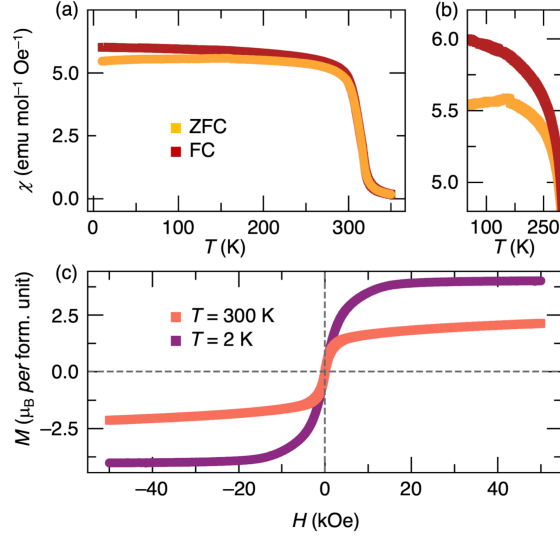
Figure 5: (a) Temperature–dependent zero field-cooled (ZFC) and field-cooled (FC) susceptibility of MnPdGa measured under a $H = 1\,\text{kOe}$ field shows a paramagnetic to ferromagnetic transition with a T_C near 310 K. (b) A selected region of the susceptibility highlighting the low temperature transition. (c) Field–dependent magnetization measurements at $T = 300\,\text{K}$ and $T = 2\,\text{K}$ demonstrate that MnPdGa is ferromagnetic. M_{sat} increases with decreasing temperature. Data were originally presented in Oey 2021.[1]

We see this bifurcation in MnPdGa (Figure 5a) and to a greater extent in MnPtGa (Figure 6a). The underlying physics of this bifurcation is similar to thermal annealing.[21] If the sample is cooled in the presence of an applied field, the domains within the sample have an external force encouraging them to align. If these domains are ferromagnetic, this leads to an increase in the magnetization; if these domains are antiferromagnetic, this leads to a decrease in the magnetization as spins anti-align. In contrast, cooling in the absence of a magnetic field, i.e. zero field cooling, does not prepare domains to co-align. The magnetization is lower in ZFC data at low temperature, as the domains require thermal energy to move domain walls and coalesce under the force of the field applied during data collection.

Ideal, e.g. totally compensated antiferromagnets do not generally exhibit FC/ZFC bifurcation, as observed in $NiTiO_3$ (Figure 4a). However, canting such that moments have small deviations from 180°correlations, glassy contributions, or particle size effects can lead to bifurcation in antiferromagnets.[26–28] Often, bifurcation in a material assumed to be
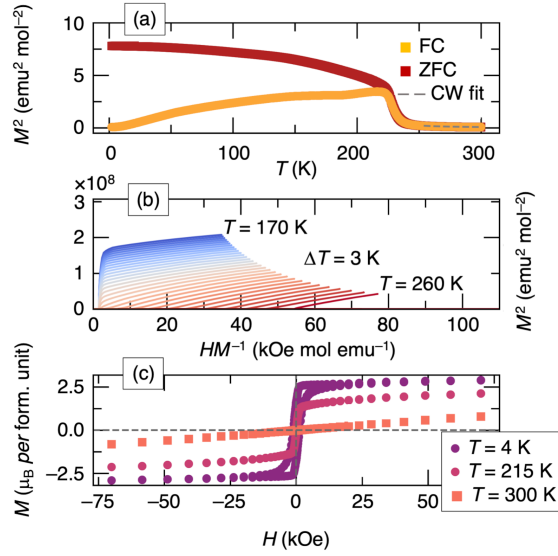
Figure 6: (a) Temperature–dependent zero field-cooled (ZFC) and field-cooled (FC) susceptibility of MnPtGa measured under a $H = 200\,\text{Oe}$ field shows a paramagnetic to ferromagnetic transition with a T_C near $230\,\text{K}$, and an additional transition near $T = 200\,\text{K}$ in the ZFC trace (near $150\,\text{K}$ in the FC trace). The Curie-Weiss fit is shown as a gray dashed line. (b) Isothermal field–dependent magnetization measurements are plotted in the Arrott style to emphasize the true T_C near $236\,\text{K}$. (c) Field–dependent magnetization measurements at $T = 300\,\text{K}$, $T = 215\,\text{K}$, and $T = 4\,\text{K}$ demonstrate that MnPtGa is a paramagnetic at $T = 300\,\text{K}$, and ferromagnetic at $T = 215\,\text{K}$ and $T = 4\,\text{K}$. Both M_{sat} and the coercive field increase with decreasing temperature.[3]

antiferromagnetic indicates a ferromagnetic component to the magnetic exchange, often termed 'weak ferromagnetism'.

In many cases estimating the T_C from a temperature-dependent magnetization does not give precise values, as the change in magnetization occurs over a temperature range. Plotting field-dependent magnetization in the Arrott style, with M^2 as the y-axis and H/M as the x-axis can make the transition more obvious as shown for MnPtGa in Figure 6b, where the dataset collected at the Curie temperature is linear with an x-intercept at the origin. It is important to collect data-sets densely over the temperature range of interest for this method.

As with antiferromagnetic materials, one can model the paramagnetic regime of a ferromagnet with the Curie-Weiss law as shown in Figure 6a for MnPtGa. Since MnPtGa transitions to the ferromagnetic state near T = 225 K, we have only fit data collected above T = 275 K. This fit gives a Θ_{CW} of 225 K which is close to the experimental value of the T_C. The Curie constant is $C = 5.7\,\mathrm{emu\,K\,mol^{-1}\,Oe^{-1}}$, meaning that $\mu_{eff} = 6.8\,\mu_B$, appreciably larger than that expected based on the total spin moment of $5.9\,\mu_B$. One explanation for this discrepancy is that in MnPtGa, the magnetism is not all local-moment and the band structure is an important consideration.

Ferromagnets have a distinctive "S" shape in the field-dependent magnetization. At high enough fields, all of the magnetic spins align and leave no opportunities for an increased magnetization at yet-higher fields, which leads to a plateau at the saturation magnetization (M_{sat}). MnPtGa and MnPdGa show linear paramagnetic behavior above T_C, and exhibit the characteristic "S" shape at temperatures below T_C (Figures 5c, 6c).[1,3] For both materials, the saturation magnetization, M_{sat} increases as temperature decreases. In MnPdGa, magnetization saturates at $2\,\mu_B$ at 300 K and then doubles to reach $4\,\mu_B$ at T=10 K.

Field-dependent magnetization shows several additional features that provide insight into the magnetic behavior of ferromagnets, highlighted in Figure 7. The saturation
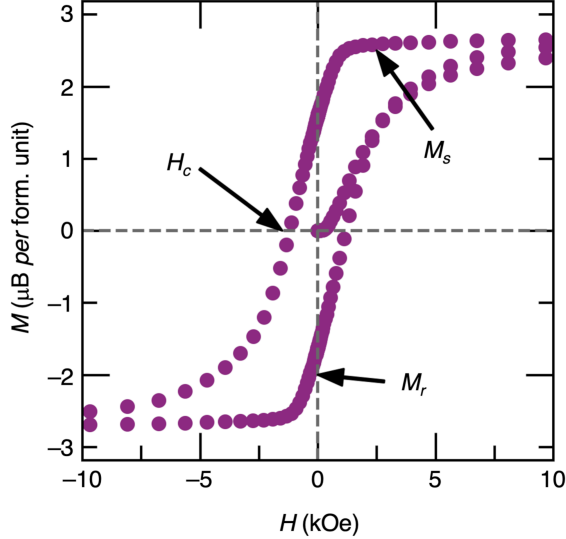
Figure 7: The field-dependent magnetization of a ferromagnet contains several important values. Here, we note the saturation magnetization (M_{sat}), the remanant magnetization (M_{rem}), and the coercive field (H_c) of MnPtGa at 4 K.

magnetization, as described above, indicates the magnetization when the spins have all aligned. The remanant magnetization, M_{rem}, is the magnetization of a sample at zero field after a field cycle. Materials with a non-zero M_{rem} are permanent magnets. Ferromagnetic materials can be characterized as hard or soft. Soft magnets have small barriers to magnetic domain reorientation and hard magnets have large barriers to domain reorientation. Hard magnets exhibit magnetic hysteresis, which is signified by the width of the curve in Figure 7. On the reverse loop, going from high fields to low fields, zero magnetization occurs at a non-zero and negative applied field. This field is called the coercive field, H_C. In MnPtGa the hysteresis loops open after the low temperature transition, as MnPtGa behaves as a soft magnet at $T = 215$ K and a hard magnet at $T = 4$ K. The distinct behavior seems to be related to the presence of the heavier Pd versus Pt; MnPdGa is a soft magnet that does not exhibit magnetic hysteresis at temperatures above $T = 2$ K in contrast to the harder magnet MnPdGa.

Ferrimagnets resemble ferromagnets in temperature-dependent and field-dependent measurements, and it can be challenging to differentiate between them with only magnetization data. The main indication of ferrimagnetic order is if the effective moment from

the M_{sat} or Curie-Weiss fit is smaller than expected for the ideal ferromagnetic state as seen in MnPdGa. Many manganese inverse Heuslers exhibit ferrimagnetism; in Mn$_2$RuGe and Mn$_2$RuGa the effective moment derived from M_{sat} is 1.55 and 0.29 μ_B per formula unit, compared to the expected $3\,\mu_B$ value for an ideal ferromagnetic configuration calculated from $2\sqrt{S \times (S+1)}$.[29] Density functional theory calculations also indicate that a ferrimagnetic state is more energetically favorable compared to a ferromagnetic state.[29] These types of discrepancies between experimental and predicted μ_{eff} values also arise in complex magnetic structures, which might involve spin canting or mesoscale spin textures. Further experiments or comparison with computation are often necessary to determine the specifics of the magnetic structure.

AC Susceptibility

AC susceptibility can provide additional details about ordering transitions.[18] In many cases χ' resembles χ_{DC}. For a ferromagnet or ferrimagnet, χ' increases at the Curie temperature and resembles χ_{DC}. An antiferromagnet exhibits a peak at the Néel temperature. χ'' can look quite different, as it captures any irreversible or sluggish behavior. Ferromagnets and ferrimagnets can often exhibit peaks in χ'', which typically are attributed to the movement of domain walls.[30] A fully compensated antiferromagnet will have no features in χ'' at the transition temperature.

This type of qualitative analysis of AC susceptibility is generally used to complement DC data that does not give conclusive results.[18] In VOSe$_2$O$_5$, AC susceptibility demonstrated that a broad feature in the DC temperature-dependent magnetization was three separate phase transitions resolvable in χ''.[31] In many skyrmion hosts, it is essential to map out the skyrmion pocket, which is made difficult by the presence of other complex magnetic phases. As shown in Figure 8a and 8b, the DC susceptibility and real AC susceptibility look very similar for the skyrmion host FePtMo$_3$N.[2] However, the AC data better resolve the double-bump feature in the $T = 230\,\text{K}$ data set that indicates a transition into and out of
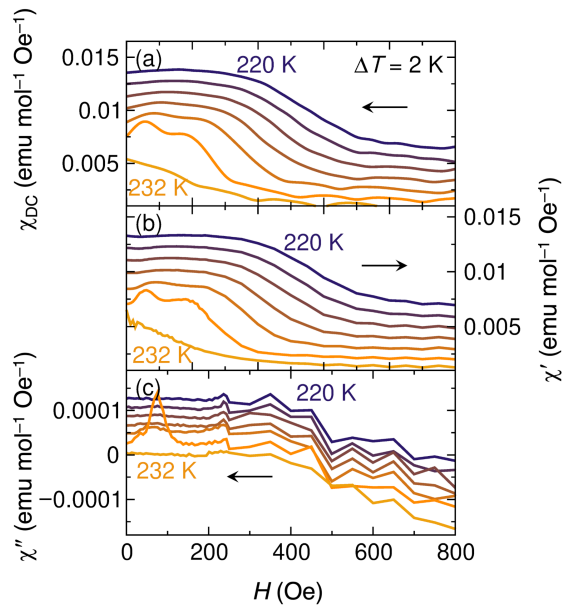
Figure 8: (a) χ_{DC} of FePtMo$_3$N as a function of applied field, where changes in slope indicate a metamagnetic transition at low fields. Data are offset by $0.001\,\mathrm{emu\,Oe^{-1}\,mol^{-1}}$ for clarity. (b) χ' as a function of applied magnetic field, which clearly shows the metamagnetic transition, collected at a frequency of $\nu = 10$Hz. Data are offset by $0.001\,\mathrm{emu\,Oe^{-1}\,mol^{-1}}$ for clarity. (c) χ'' as a function of applied magnetic field, collected at a frequency of $\nu = 10\,$Hz. Data are offset by $0.00002\,\mathrm{emu\,Oe^{-1}\,mol^{-1}}$ for clarity. Data were originally presented in Kautzsch 2020.[2]

the skyrmion phase. Although the low signal associated with the imaginary susceptibility relative to the real and DC susceptibilities renders the data fairly noisy, we can still observe features that indicate that the low field transition exhibits losses in 8c. Since this feature correlates to the entrance and exit out of the skyrmion state, it suggests that these losses are related to the motion of large magnetic objects on slow timescales. In $FePtMo_3N$, the AC susceptibility was more sensitive to the magnetic transition of interest, and provided additional evidence for the presence of large magnetic bodies.

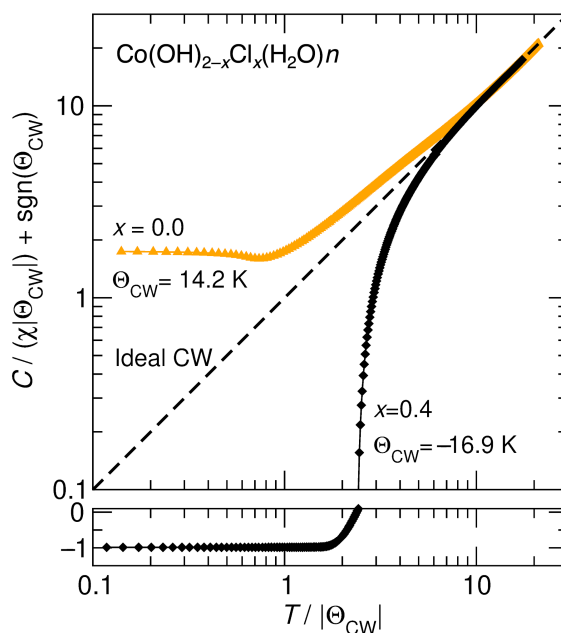## Comparing ferromagnets and antiferromagnets on the same plot

Figure 9: The inverse susceptibility as a function of temperature for several members of the series $Co(OH)_{(2-x)}Cl_x(H_2O)_n$ scaled according to Equation 5. Ideal Curie-Weiss paramagnetism ($\Theta_{CW} = 0$) is shown as a black dashed line. Positive deviations from this line indicate compensated interactions, *e.g.* antiferromagnetism, while negative deviations indicate uncompensated interactions, *e.g.* ferromagnetism or ferrimagnetism. Data were originally presented in Neilson 2011.[32]

Comparing the temperature-dependent behavior of distinct magnetic materials on the same plot can be challenging if there are a range of transition temperatures and varying magnitudes of the susceptibility. A useful method to employ is to first fit the higher-

temperature data data to the Curie-Weiss law and extract for each data set a reliable value of C and Θ_{CW}. These values are then used to normalize the susceptibility data at all temperatures in the following manner: If we express the Curie-Weiss law as the inverse susceptibility, $1/\chi = (T - \Theta_{CW})/C$, then multiplying both sides by C and dividing by the absolute value of Θ_{CW} gives

$$\frac{C}{\chi|\Theta_{CW}|} + sgn(\Theta_{CW}) = \frac{T}{\Theta_{CW}} \tag{5}$$

where $sgn(x)$ returns values of -1 or $+1$ for negative or positive Θ_{CW}. Figure 9 shows this relationship for several members of the series $Co(OH)_{(2-x)}Cl_x(H_2O)_n$. When $x = 0.0$, the sample deviates positively from the ideal Curie-Weiss paramagnetism to suggest compensated spins, and when $x = 0.4$, the deviation from the ideal Curie-Weiss paramagnetism is negative suggesting uncompensated spins.[32] These evolution of the data suggests a transition from ferrimagnetic to antiferromagnetic ordering as x increases, and that is readily apparent in Figure 9.

Calculating entropy

The entropic contribution to a magnetic phase transition has wide application and is particularly important in materials of interest for magnetocaloric refrigeration. Magnetocaloric refrigeration typically relies on a ferromagnetic material, held close to its Curie temperature. The distinct entropic states of the magnetic material when the spins are aligned under an applied field (the low entropy state) and when the spins are misaligned upon removal of the field (the high-entropy state) are reminiscent of changes in the fluids used in vapor-compression refrigeration. Cycles of isothermal and adiabatic magnetization and demagnetization can enable magnetic refrigeration. With the appropriate heat transport elements, this magnetocaloric effect can thereby be used to remove heat from a system.[33] The efficacy of this process relies on the magnitude of the entropy change of the material
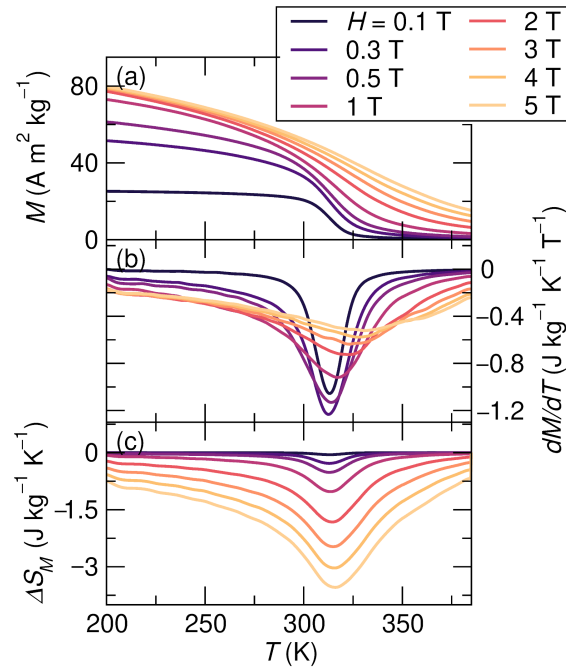
Figure 10: Process of transforming the temperature-dependent magnetization to isothermal entropy upon magnetization. (a) Temperature-dependent magnetization of MnPdGa collected for a range of fields. (b) Differentiated temperature-dependent magnetization of MnPdGa shows a peak at the transition temperature. (c) Isothermal entropy upon magnetization of MnPdGa, calculated from Equation 7. Data were originally presented in Oey 2021.[1]

under an applied field, and knowing ΔS_M is essential for complete characterization for candidate materials.

In Figure 10, we show the process of calculating ΔS_M, the magnetic entropy change, from temperature-dependent magnetization for MnPdGa, which has a Curie temperature near $T = 310$ K. This transition is evident in the temperature-dependent magnetization, although the feature broadens with increasing applied field. This broadening is reflected in the differentiated data-sets in Figure 10b, which show a narrow discontinuity at low fields that broadens to a feature that is tens of K wide. Appropriate integration, described below, of the data in Figure 10b yields the gravimetric ΔS_M values up to 3.54 J kg^{-1} K^{-1} (Figure 10c). Since palladium is such a heavy metal, it is worth considering the volumetric ΔS_M, which is 30.1 mJ cm^{-3} K^{-1}. The refrigerant capacity (RC) is defines as the area under the ΔS_M curve truncated at the full-width half-maximum (FWHM). It is a useful metric for magnetocalorics. Under a $H = 2$ T applied field, the FHWM is 60 K, spanning $T = 279$ K to $T = 339$ K which leads to a refrigerant capacity of RC = 85.1 J kg^{-1} for MnPdGa. It is valuable to calculate all three metrics, for best comparison with literature.

The Maxwell relation:

$$(\frac{\partial S}{\partial H})_T = (\frac{\partial M}{\partial T})_H \tag{6}$$

where S is the total entropy, M is the magnetization, H is the applied field, and T is the temperature demonstrates how the change in entropy across a given transition can be obtained from field dependent magnetization. The isothermal entropy change under magnetization (ΔS_M) can be expressed as:

$$\Delta S_M(T, H) = \int_0^H (\frac{\partial M}{\partial T})_{H'} \, dH' \tag{7}$$

Therefore, by collecting a series of field-dependent magnetization datasets, differentiating them, and then integrating according to equation 7 the magnetic entropy contribution can be calculated for a phase transition. Annotated python codes to perform this analysis as in

27

Figure 10 are available in the supplementary information of Bocarsly *et. al.*[34]

In addition to applications in magnetocalorics, it has recently been demonstrated that transforming the magnetization as a function of temperature to isothermal magnetic entropy change can be used to rapidly prepare a magnetic phase diagram.[34] This is especially useful for the detection of states like skyrmions and helical magnetism that yield only small anomalies in the original magnetization or susceptibility but have large entropic signatures. For example, the phase diagram of the skymrion host FeGe had been contested and it remained unclear whether there was one sykrmion phase or several. By collecting the temperature-dependent magnetization at a range of fields and transforming them into ΔS_M we were able to calculate a thermodynamic phase diagram that showed a single skyrmion phase (Figure 11b).[34] For this application, it is important to collect data at sufficiently small magnetic field spacing as to capture all relevant features.

Spin glass formation

A spin glass is characterized by the frustration of long range magnetic order because of underlying compositional disorder in the material, while retaining short range correlations that result in spin-freezing.[35,36] Above the freezing temperature T_f, spins are dynamic in a paramagnetic state. On cooling through T_f the spins freeze into a disordered state with only short-range correlations. The correlation lengths found in the states where the spins communicate with one-another can determine the different degrees of "glassiness".[6,37]

Frequency-dependence in AC susceptibility is consider the most reliable method for observing the formation of a spin glass, but DC measurements provide preliminary evidence when a spin glass is unexpected or AC measurements are unavailable.[38] A broad hump in the temperature-dependent DC susceptibility or an off-centering of a field-dependent magnetization collected below T_f are the primary features that suggest glassiness.[6,39,40]

Another indication of spin glass behavior is geometric frustration, indicated by a disagreement between the measured Curie temperature and Θ_{CW} obtained from Curie-Weiss
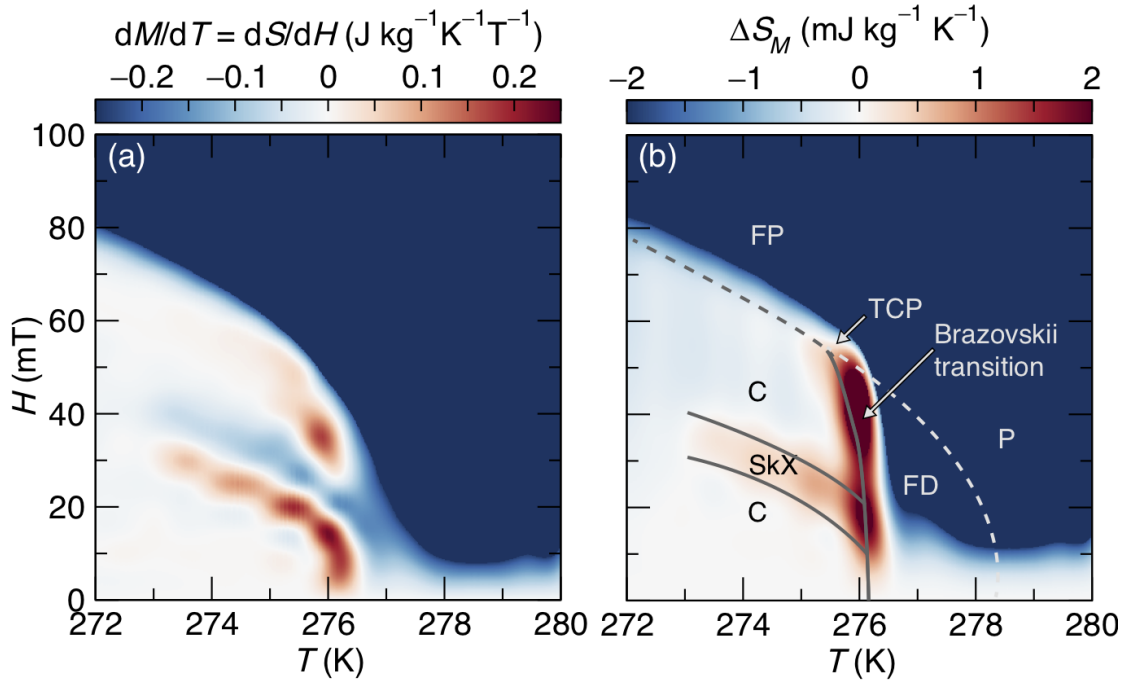
Figure 11: (a) Map of the magnetic susceptibility of FeGe differentiated numerically in the temperature range close to the skyrmion phase transition. (b) Integration according to equation 7 gives the map of $\Delta S_M(T, H)$ for FeGe, which shows the skyrmion pocket (SkX) as a region of high entropy relative to the field polarized (FP), fluctuation disordered (FD), paramagnetic (P), and conical (C) regions. TCP indicates the tri-critical point. Reprinted with permission from Bocarsly, Need, Seshadri Wilson *Physical Review B* 97, 100404(R) 2018. Copyright 2018 by the American Physical Society.[34]

fits to the high-temperature data. The disagreement is often expressed as a frustration index $f = (\Theta_{CW}/T_C)$.[4] In materials that are not frustrated, the measured transition temperature and the Curie temperature calculated from fitting to the Curie law will be similar. In $Co(OH)_{(2-x)}Cl_xH_2O_n$ the frustration index is very close to one, evidenced by the temperature axis in Figure 9, which suggests a lack of frustration. In contrast, in the spinels $ZnCr_2O_4$, $CoCr_2O_4$, and their solid solution series, Θ_{CW} is between 8 and 51 times larger than the experimental ordering temperature.[41] Correspondingly, the DC magnetic susceptibility of these spinels exhibit broad features consistent with spin glass behavior at low temperatures.

In $Co_7Zn_7Mn_6$, a gradual decrease after the Curie temperature to an eventual plateau in the DC susceptibility and hysteresis in the DC field-dependent magnetization hint at glassy behavior.[6] As shown in Figure 12a, χ' appears very similar to χ_{DC} at high temperatures. However, at low temperature the decrease in χ' is far more pronounced. χ'' exhibits a sharp feature at $T = 30\,\text{K}$ that coincides with the decrease in χ' and χ_{DC} (Figure 12c). The sharpness of the peak in χ'' makes it easy to determine an accurate transition temperature. Both the decrease in χ' and the peak in χ'' are frequency dependent (Figure 12b and 12d), confirming the formation of a glassy state. The relative shift in freezing temperature per decade of AC field frequency ν is suggestive of the length scale of correlations and can be captured as $\delta T_f = \Delta T_f/[T_f \Delta \log_{10}(\nu/Hz)]$. Dilute spin glasses like the archetypal Cu_xMn_{1-x} have δT_f values around 0.005, while the cluster glass $Co_7Zn_7Mn_6$ has $\delta T_f = 0.038$, an order of magnitude larger.[4,6]

Superconductors

Superconductors displaying the Meissner effect expel magnetic field, behaving as perfect diamagnets when cooled to below their critical temperature.[11] At the superconducting transition, the susceptibility will decrease to a constant, negative value. However, a high enough magnetic field will overpower the perfect diamagnetism of a superconductor. Pb
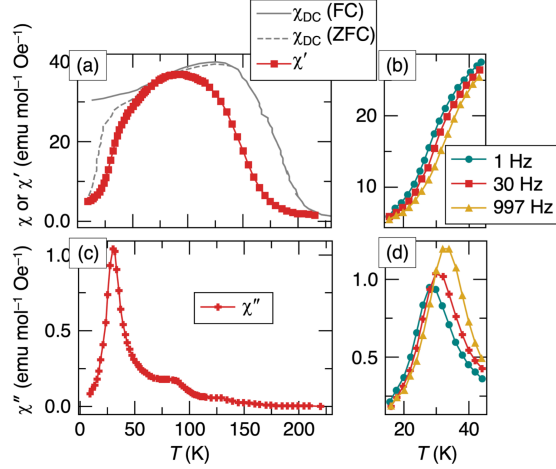
Figure 12: (a) χ_{DC} and the χ' for Co$_7$Zn$_7$Mn$_6$ as a function of temperature (b) χ' measured at various frequencies demonstrates the frequency dependence of the observed transition.(c) χ'' as a function of temperature. (d) χ'' measured at various frequencies demonstrates the frequency dependence of the observed transition. Data were originally presented in Bocarsly 2018.[6]

becomes superconducting below $T = 10$ K (Figure 13). This transition manifests as the abrupt disconitinuity in susceptibility at $T = 7$ K for data collected under an $H = 100$ Oe field. At higher magnetic fields, this transition is suppressed and exhibits lower superconducting transition temperatures and shallower slopes to the minimum susceptibility. When an $H = 800$ Oe field is applied to the lead sample, no anomaly indicating a superconducting transition is seen down to base temperature. The field at which the superconducting transition disappears is known as the critical field. These data indicate that the critical field for lead is between 700 Oe and 800 Oe.

Qualitative observation of the behavior of a superconductor under magnetic field allows us to describe them either as type-I superconductors, like lead, that have one critical field or as type-II superconductors.[11] Rather than completely allowing the magnetic field to penetrate, in type-II superconductors like vanadium and the cuprates, vortices form at the first critical field that allow the field to penetrate the material without increasing the bulk resistivity. Increasing the field again past the second critical field will then destroy the superconducting state.
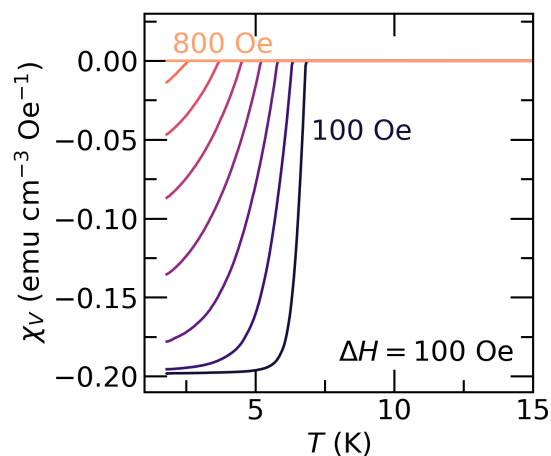
31

Figure 13: Volume susceptibility as a function of temperature of lead powder at various fields in the vicinity of the superconducting transition. Increasing the applied field towards the critical field suppresses the superconducting transition.
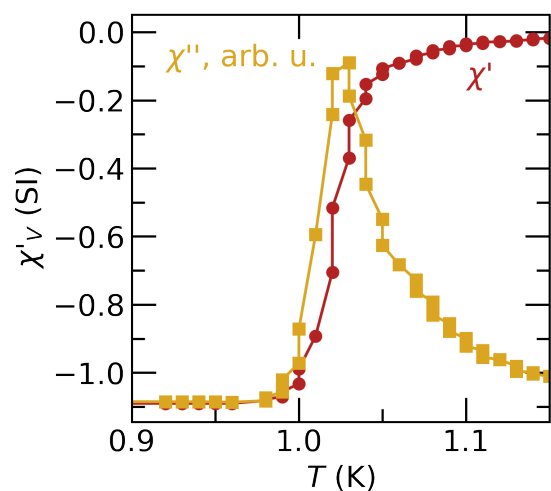

Figure 14: Low temperature AC susceptibility measurements of KV_3Sb_5 show the onset of bulk superconductivity. Data were originally presented in Ortiz *et al.*.[42]

AC susceptibility measurements have been widely used to confirm the presence of a superconducting state, and to determine the critical temperature. The real susceptibility shows the same transition to a diamagnetic state as the DC susceptibility. The superconducting transition also involves the movement of domain walls and other irreversible processes, and is often accompanied by a peak in the imaginary susceptibility. Just as in spin glasses, the peak in the imaginary susceptibility accurately depicts the transition temperature. These features are shown for KV_3Sb_5 in Figure 14.[42]

Complementary techniques

Thus far, we have focused on data obtained from a magnetometer, which serves only as a beginning for the characterization of magnetic materials. In cases where AC and DC measurements suggest the presence of more complex magnetic ground states than a simple ferromagnet or antiferromagnet, such as the low temperature transitions of MnPdGa and MnPtGa (Figures 5, 6) , additional techniques can provide valuable insight. We provide two case studies below that demonstrate how neutron diffraction and Mössbauer spectroscopy can be used to answer questions raised by magnetometer measurements. We would be remiss if we did not mention that nuclear magnetic resonance, electron spin resonance, and muon spin spectroscopies can be used to gain insight into local environments and spin dynamics in magnetic materials. These techniques and their applications have been more thoroughly reviewed elsewhere.[43–45]

Neutron diffraction

Neutron diffraction is a useful complementary technique to investigate the spatial ordering of moments in magnetically ordered materials. Neutrons possess a magnetic moment and their scattering is strongly influenced by organized magnetic moments on atoms in the materials they scatter from.[46] If the magnetic structure and nuclear structure are com-
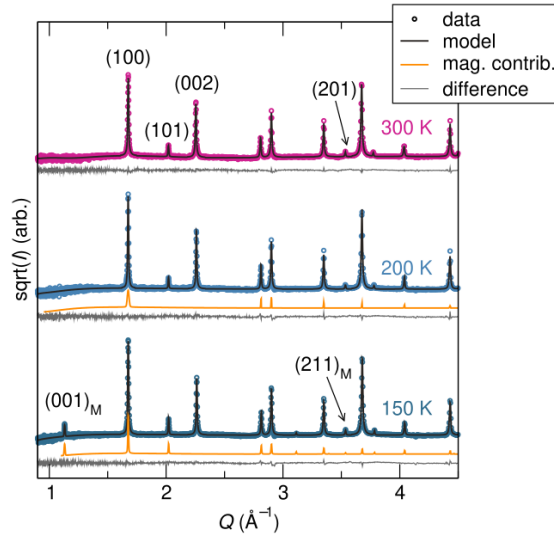
Figure 15: Magnetic Rietveld refinements of neutron diffraction data collected of MnPtGa using center wavelength 2.665 Å on the POWGEN diffractometer at $T = 300\,\mathrm{K}$, $T = 200\,\mathrm{K}$, and $T = 150\,\mathrm{K}$. The $T = 300\,\mathrm{K}$ pattern contains only nuclear intensity, the $T = 200\,\mathrm{K}$ pattern shows the addition of additional magnetic intensity on the nuclear peaks, and the $T = 150\,\mathrm{K}$ pattern shows new magnetic Bragg reflections. Data were originally presented in Cooley 2020.[3]

mensurate, the magnetic component of the diffraction patterns will manifest as additional intensity in the relevant Bragg features. If there is symmetry reduction between the nuclear and the magnetic structure (*i.e.* symmetry breaking resulting from spin canting or antiferromagnetic order) then additional Bragg reflections will be resolved.

In MnPtGa, both commensurate and symmetry-breaking features are observed (Figure 15). Data collected above the magnetic ordering temperature can be modeled with only the nuclear density. At $T = 200\,\mathrm{K}$, several Bragg features display intensities that cannot be captured by the nuclear structure alone, which is consistent with the ferromagnetic order indicated by the magnetometry. The additional intensity can be modeled quite well in the Rietveld refinement as a magnetic phase with ferromagnetic ordering. Below the low temperature transition, several additional Bragg reflections are resolved at low scattering vectors Q, indicating complexity in the magnetic structure that is not reflected in the nuclear structure. The presence of multiple reflections indicate that this is not a simple structural change, and were attributed to a non-collinear arrangement of magnetic spins,

culminating in the formation of a spin wave at the lowest temperature studied.

In some cases, the nuclear structure also changes at low temperature. Comparison of low temperature X-ray or electron diffraction with the neutron diffraction data confirms whether reflections are due to the magnetic structure. In materials with larger magnetic features, such as long wavelength spin waves or skyrmions, diffraction experiments do not access a short enough region in reciprocal space. Small angle neutron scattering is often used in these cases.[47]

Mössbauer spectroscopy

Mössbauer spectroscopy is an absorption technique, using gamma rays of appropriate energies to interact with the nucleus of an atom.[48] It is best used on crystalline solids, since the rigid framework will prevent the nuclei from recoiling when interacting with gamma rays. The source that emits gamma rays must be the same isotope as the one of interest in the sample so the emitted gamma rays have the appropriate energies. The emitted gamma rays are detected by moving the source and measuring the Doppler shift. Mössbauer spectra are therefore typically reported in reference to a velocity. A limitation of this technique is that the number of suitable isotopes with appropriate half-lives that can serve as gamma ray sources are limited, as are the number of nuclear transitions that have the correct lifetimes for the technique to be effective. Most spectra are collected in transmission geometry and require sufficiently thin samples.

If the source atoms and the sample ions are in identical environments, then the gamma ray will be absorbed and emitted without any change in energy. Changes to the local environment that will manifest in Mössbauer spectra fit into three distinct categories. First, the isomer shift depends on the electron density outside the nucleus as the electrons coulombically modify the nuclear energy levels. The isomer shift manifests as shift of the peak center, and is useful to determine oxidation states. Second, a nucleus with a non-spherical nuclear density, *i.e.* with an angular orbital momentum (l) greater than one half, will have

a nuclear quadrupole moment that will split a given feature into doublets or triplets depending on the l value, informing on spin states in the system. Third, the magnetic field exerted on the nucleus from unpaired electrons under an applied field will lead to hyperfine magnetic splitting according to the Zeeman field, helping to establish that compound is magnetically ordered.
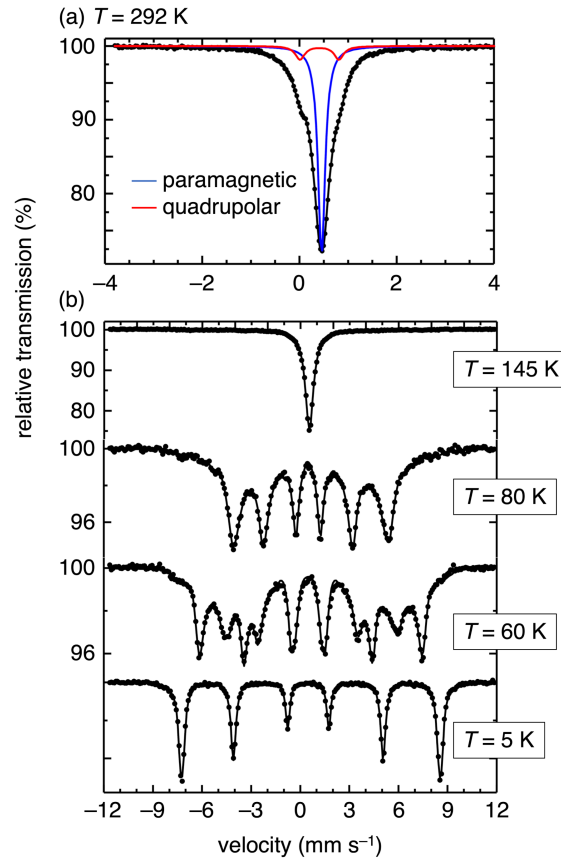

Figure 16: (a) Mössbauer spectrum of Sr_2FeOsO_6 at room temperature showing a single feature with shoulders on the high and low velocity regions. The data can be modeled with a single paramagnetic feature and a minor quadrupolar contribution. (b) Mössbauer spectra of Sr_2FeOsO_6 as a function of temperature shown as dots with solid lines representing the calculate spectra. Reprinted figure with permission from Adler, Medvedev, Naumov, Mohitkar, Rüffer, Jansen, and Felser, *Phys. Rev. B*, 99, 134443, 2019. Copyright 2019 by the American Physical Society.

In the Mössbauer spectrum of a magnetic material, all three interactions are at play, with differing levels of impact on the data, as we will demonstrate for Sr_2FeOsO_6 (Figure 16). $SrFeOsO_6$ exhibits unusual magnetic behavior; Goodenough-Kanamori rules and

Curie fits to the high temperature magnetization suggest that it should be a ferromagnet, but it undergoes two antiferromagnetic transitions between $T = 50\,K$ and $T = 200\,K$.[49] From magnetometry data, it remained unclear what spin textures these transitions involved, and why the higher-temperature feature was so broad. Mössbauer spectroscopy answers some of these questions.[50]

At high temperature, the Mössbauer spectrum exhibits one feature, which has shoulders on either side. The shoulders on the peak indicate that there are at least two iron sites in this material that each give rise to a different characteristic energy or velocity. Fitting of the spectra demonstrates that the second component exhibits quadrupole splitting, which the authors attribute to structural distortions from site swapping of the iron and osmium. The singlet feature has an isomer shift of $0.455\,mm\ s^{-1}$ relative to the source, and the doublet feature an isomer shift of $0.80\,mm\ s^{-1}$ indicative of the difference in electron density around iron in each environment.

The spectrum looks fairly similar at 145 K, although the shoulders are not as well resolved. Below the magnetic ordering temperatures, several additional features are observed, for a total of six peaks that is consistent with Fe^{3+}. At 5 K, these features are narrow and appear to be the only contribution to the spectrum. The space between the components of the sextet give a hyperfine field of 49 T. The spectra collected at 80 K and 60 K exhibit this same sextet, but there is also an additional broad feature that has a hyperfine field of 33 T. The breadth of this feature suggests that the higher temperature antiferromagnetic phase is frustrated, but this frustration is relieved at temperatures below the second antiferromagnetic transition. Additional neutron diffraction studies are consistent with this hypothesis.[51] In this case study, Mössbauer spectroscopy revealed disorder and glassy behavior that provided valuable insight into magnetometry experiments.

Conclusion

Developing expertise with a new technique is an integral part of research, whether one is a new graduate student or an established principal investigator. While user manuals, textbooks, and literature results provide valuable insights into techniques, often there is gap that hampers mastery without intervention of an expert. Magnetic measurements are an excellent example of this type of technique. Insightful analysis requires careful sample preparation, judicious choice of experimental parameters, and thoughtful presentation of data. The results are impactful across disciplines. When done correctly, magnetometry can be used to identify the charge state of battery materials, characterize magnetic ground states, elucidate the extent of magnetic order, and classify superconductors. We consider this contribution as an ettempt to demystify magnetic characterization, particularly for those whose research is not centrally based around characterizing magnetic materials.

Acknowledgements:

References

(1) Oey, Y. M.; Kitchaev, D. A.; Bocarsly, J. D.; Schueller, E. C.; Cooley, J. A.; Seshadri, R. Magnetocaloric Behavior and Magnetic Ordering in MnPdGa. *Phys. Rev. Mat.* **2021**, *5*, 014414.

(2) Kautzsch, L.; Bocarsly, J. D.; Felser, C.; Wilson, S. D.; Seshadri, R. Con-

trolling Dzyaloshinskii-Moriya Interactions in the Skyrmion Host Candidates FePd$_{1-x}$Pt$_x$Mo$_3$N. *Phys. Rev. Mat.* **2020**, *4*, 024412.

(3) Cooley, J. A.; Bocarsly, J. D.; Schueller, E. C.; Levin, E. E.; Rodriguez, E. E.; Huq, A.; Lapidus, S. H.; Wilson, S. D.; Seshadri, R. Evolution of Noncollinear Magnetism in Magnetocaloric MnPtGa. *Phys. Rev. Mat.* **2020**, *4*, 044405.

(4) Ramirez, A. Strongly Geometrically Frustrated Magnets. *Ann. Rev. Mater. Sci.* **1994**, *24*, 453–480.

(5) Preefer, M. B.; Saber, M.; Wei, Q.; Bashian, N. H.; Bocarsly, J. D.; Zhang, W.; Lee, G.; Milam-Guerrero, J.; Howard, E. S.; Vincent, R. C.; Melot, B. C.; Van der Ven, A.; Seshadri, R.; Dunn, B. S. Multielectron Redox and Insulator-to-Metal Transition upon Lithium Insertion in the Fast-Charging, Wadsley-Roth Phase PNb$_9$O$_{25}$. *Chem. Mater.* **2020**, *32*, 4553–4563.

(6) Bocarsly, J. D.; Heikes, C.; Brown, C. M.; Wilson, S. D.; Seshadri, R. Deciphering Structural and Magnetic Disorder in the Chiral Skyrmion Host Materials Co$_x$Zn$_y$Mn$_z$ ($x + y + z = 20$). *Phys. Rev. Mat.* **2019**, *3*, 014402.

(7) Cullity, B. D.; Graham, C. D. *Introduction to Magnetic Materials*; John Wiley and Sons, Inc., 2008.

(8) Woodward, P. M.; Karen, P.; Evans, J. S. O.; Vogt, T. *Solid State Materials Chemistry*; Cambridge University Press, 2021.

(9) Chilton, N. F. Molecular Magnetism. *Annu. Rev. Mater. Res.* **2022**, *52*, 79–101.

(10) Willard, M.; Kurihara, L.; Carpenter, E.; Calvin, S.; Harris, V. Chemically Prepared Magnetic Nanoparticles. *Int. Mater. Rev.* **2004**, *49*, 125–170.

(11) Spaldin, N. A. *Magnetic Materials: Fundamentals and Applications*, 2nd ed.; Cambridge University Press, 2011; pp 42–46.

(12) Abraham, D. W.; Frank, M. M.; Guha, S. Absence of Magnetism in Hafnium Oxide Films. *Appl. Phys. Lett.* **2005**, *87*, 252502.

(13) Beille, J.; Bloch, D.; Besnus, M. J. Itinerant Ferromagnetism and Susceptibility of Nickel-Platinum Alloys. *J. Phys. F* **1974**, *4*, 1275–1284.

(14) Hoare, F. E.; Matthews, J. C.; Stoner, E. C. The Magnetic Susceptibilities of Platinum, Rhodium and Palladium from 20 to 290 K. *Proc. Math. Phys. Eng. Sci.* **1952**, *212*, 137–148.

(15) Yan, J.-Q.; Zhang, Q.; Heitmann, T.; Huang, Z.; Chen, K. Y.; Cheng, J.-G.; Wu, W.; Vaknin, D.; Sales, B. C.; McQueeney, R. J. Crystal growth and magnetic structure of $MnBi_2Te$. *Physical Review Materials* **2019**, *3*, 064202.

(16) Kong, T.; Guo, S.; Ni, D.; Cava, R. J. Crystal structure and magnetic properties of the layered van der Waals compound VBr_3. *Physical Review Materials* **2019**, *3*, 084419.

(17) Topping, C. V.; Blundell, S. J. A.C. susceptibility as a probe of low-frequency magnetic dynamics. *Journal of Physics: Condensed Matter* **2019**, *31*, 013001.

(18) Aharoni, A.; Wohlfarth, E. P. The isothermal remanence (IRM) and the thermoremanence (TRM) of spin glasses. *Journal of Applied Physics* **1984**, *55*, 1664–1666.

(19) Foner, S. Versatile and Sensitive Vibrating-Sample Magnetometer. *Review of Scientific Instruments* **1959**, *30*, 548–557.

(20) Ortiz, B. R.; Teicher, S. M.; Hu, Y.; Zuo, J. L.; Sarte, P. M.; Schueller, E. C.; Abeykoon, A. M.; Krogstad, M. J.; Rosenkranz, S.; Osborn, R.; Seshadri, R.; Balents, L.; He, J.; Wilson, S. D. CsV_3Sb_5: A Z2 Topological Kagome Metal with a Superconducting Ground State. *Phys. Rev. Lett.* **2020**, *125*, 247002.

(21) Joy, P. A.; Kumar, P. S. A.; Date, S. K. The relationship between field-cooled and zero-field-cooled susceptibilities of some ordered magnetic systems. *Journal of Physics: Condensed Matter* **1998**, *10*, 11049–11054.

(22) Mugiraneza, S.; Hallas, A. M. Tutorial: A Beginner's Guide to Interpreting Magnetic Susceptibility Data with the Curie-Weiss law. *Commun. Phys.* **2022**, *5*, 95.

(23) Raychaudhuri, D, P.; Sengupta, P. N. Studies on Constant Paramagnetism, Part 1. **1936**, *10*, 245–251.

(24) Carrington, A. The Temperature-Independent Paramagnetism of Permanganate and Related Complexes. *Mol. Phys.* **1960**, *3*, 271–275.

(25) Harada, J. K.; Balhorn, L.; Hazi, J.; Kemei, M. C.; Seshadri, R. Magnetodielectric Coupling in the Ilmenites MTiO$_3$ ($M =$Co, Ni). *Phys. Rev. B* **2016**, *93*, 104404.

(26) Liu, X.; Taddei, K. M.; Li, S.; Liu, W.; Dhale, N.; Kadado, R.; Berman, D.; Cruz, C. D.; Lv, B. Canted antiferromagnetism in the quasi-one-dimensional iron chalcogenide BaFe$_2$Se. *Physical Review B* **2020**, *102*, 180403.

(27) Nambu, Y.; Macaluso, R. T.; Higo, T.; Ishida, K.; Nakatsuji, S. Structural properties of the two-dimensional triangular antiferromagnet NiGa$_2$S. *Physical Review B* **2009**, *79*, 214108.

(28) Gnewuch, S.; Rodriguez, E. E. Distinguishing the Intrinsic Antiferromagnetism in Polycrystalline LiCoPO$_4$ and LiMnPO$_4$ Olivines. *Inorganic Chemistry* **2020**, *59*, 5883–5895.

(29) Yang, L.; Liu, B.; Meng, F.; Liu, H.; Luo, H.; Liu, E.; Wang, W.; Wu, G. Magnetic Properties of Heusler Alloy Mn$_2$RuGe and Mn$_2$RuGa Ribbons. *J. Magn. Magn. Mater.* **2015**, *379*, 1–5.

(30) Yoon, S. S.; Kim, C. Q. Separation of Reversible Domain-Wall Motion and Magnetization Rotation Components in Susceptibility Spectra of Amorphous Magnetic Materials. *Appl. Phys. Lett.* **2001**, *78*, 3280–3282.

(31) Kim, S. H.; Halasyamani, P. S.; Melot, B. C.; Seshadri, R.; Green, M. A.; Sefat, A. S.; Mandrus, D. Experimental and Computational Investigation of the Polar Ferrimagnet VOSe$_2$O$_5$. *Chem. Mater.* **2010**, *22*, 5074–5083.

(32) Neilson, J. R.; Morse, D. E.; Melot, B. C.; Shoemaker, D. P.; Kurzman, J. A.; Seshadri, R. Understanding Complex Magnetic Order in Disordered Cobalt Hydroxides through analysis of the local Structure. *Phys. Rev. B* **2011**, *83*, 094418.

(33) Franco, V.; Blázquez, J.; Ingale, B.; Conde, A. The Magnetocaloric Effect and Magnetic Refrigeration Near Room Temperature: Materials and Models. *Annu. Rev. Mater. Res.* **2012**, *42*, 305–342.

(34) Bocarsly, J. D.; Need, R. F.; Seshadri, R.; Wilson, S. D. Magnetoentropic Signatures of Skyrmionic Phase Behavior in FeGe. *Phys. Rev. B* **2018**, *97*, 100404.

(35) Sherrington, D. A spin glass perspective on ferroic glasses. *physica status solidi (b)* **2014**, *251*, 1967–1981.

(36) Binder, K.; Young, A. P. Spin glasses: Experimental facts, theoretical concepts, and open questions. *Reviews of Modern Physics* **1986**, *58*, 801–976.

(37) Mydosh, J. Disordered magnetism and spin glasses. *Journal of Magnetism and Magnetic Materials* **1996**, *157-158*, 606–610.

(38) Shoemaker, D. P.; Rodriguez, E. E.; Seshadri, R.; Abumohor, I. S.; Proffen, T. Intrinsic exchange bias in Zn$_x$Mn$_{\{3-x\}}$O$_4$ $x < 4$ solid solutions. *Physical Review B* **2009**, *80*, 144422.

(39) Li, D. X.; Shiokawa, Y.; Homma, Y.; Uesawa, A.; Dönni, A.; Suzuki, T.; Haga, Y.; Yamamoto, E.; Honma, T.; Ōnuki, Y. Evidence for the formation of the spin-glass state in U_2PdSi_3. *Physical Review B* **1998**, *57*, 7434–7437.

(40) Mulder, C. A. M.; van Duyneveldt, A. J.; Mydosh, J. A. Frequency and field dependence of the ac susceptibility of the AuMn spin-glass. *Physical Review B* **1982**, *25*, 515–518.

(41) Melot, B. C.; Drewes, J. E.; Seshadri, R.; Stoudenmire, E. M.; Ramirez, A. P. Magnetic Phase Evolution in the Spinel Compounds $Zn_{1-x}Co_xCr_2O_4$. *J. Condens. Matter Phys.* **2009**, *21*, 216007.

(42) Ortiz, B. R.; Sarte, P. M.; Kenney, E. M.; Graf, M. J.; Teicher, S. M. L.; Seshadri, R.; Wilson, S. D. Superconductivity in the Z2 Kagome Metal KV_3Sb_5. *Phys. Rev. Mat.* **2021**, *5*, 034801.

(43) Grey, C. P.; Dupré, N. NMR Studies of Cathode Materials for Lithium-Ion Rechargeable Batteries. *Chem. Rev.* **2004**, *104*, 4493–4512.

(44) Pell, A. J.; Pintacuda, G.; Grey, C. P. Paramagnetic NMR in Solution and the Solid State. *Prog. Nucl. Magn. Reson. Spectrosc.* **2019**, *111*, 1–271.

(45) Nuccio, L.; Schulz, L.; Drew, A. J. Muon Spin Spectroscopy: Magnetism, Soft matter and the Bridge Between the Two. *J. Phys. D* **2014**, *47*, 473001.

(46) Bacon, G. E. G. E. *Neutron diffraction*; Clarendon Press, 1975; p 636.

(47) Mühlbauer, S. S.; Binz, B.; Jonietz, F.; Pfleiderer, C.; Rosch, A.; Neubauer, A.; Georgii, R.; Böni, P. Skyrmion Lattice in a Chiral Magnet. *Science* **2011**, *333*, 1381.

(48) Gager, H. M.; Jr., M. C. H. Mössbauer Spectroscopy. *Catalysis Reviews* **1975**, *11*, 117–166.

(49) Paul, A. K.; Jansen, M.; Yan, B.; Felser, C.; Reehuis, M.; Abdala, P. M. Synthesis, Crystal Structure, and Physical Properties of Sr_2FeOsO_6. *Inorg. Chem.* **2013**, *52*, 6713–6719.

(50) Adler, P.; Medvedev, S. A.; Naumov, P. G.; Mohitkar, S.; Rüffer, R.; Jansen, M.; Felser, C. High-Pressure Magnetism of the Double Perovskite Sr_2FeOsO_6 Studied by Synchrotron [57]Fe Mössbauer Spectroscopy. *Phys. Rev. B* **2019**, *99*, 134443.

(51) Taylor, A. E.; Morrow, R.; Lumsden, M. D.; Calder, S.; Upton, M. H.; Kolesnikov, A. I.; Stone, M. B.; Fishman, R. S.; Paramekanti, A.; Woodward, P. M.; Christianson, A. D. Origin of Magnetic Excitation Gap in Double Perovskite Sr_2FeOsO_6. *Phys. Rev. B* **2018**, *98*, 214422.

TOC Graphic